Supplementary Information

Hybrid Superlattice Cathodes Unlocking Diffusion-Barrier-Free Proton Storage for Ultrahigh-Rate Zn-MnO_2 Batteries

Yumin Chen, Da Zhang, Chengmin Hu, Pingxuan Liu, Xiaozhe Yang, Hui Duan, Ling Miao, Yaokang Lv, Ziyang Song,* Lihua Gan,* Mingxian Liu*

Y. Chen, D. Zhang, P. Liu, X. Yang, Dr. H. Duan, Dr. L. Miao, Dr. Z. Song, Prof. L. Gan, Prof. M. Liu

Shanghai Key Lab of Chemical Assessment and Sustainability, School of Chemical Science and Engineering, Tongji University, 1239 Siping Rd., Shanghai, 200092, P. R. China. *E-mail: 21310240@tongji.edu.cn (Z. Song), ganlh@tongji.edu.cn (L. Gan), liumx@tongji.edu.cn (M. Liu).

Prof. L. Gan, Prof. M. Liu

State Key Laboratory of Cardiovascular Diseases and Medical Innovation Center, Shanghai East Hospital, School of Medicine, Tongji University, 150 Jimo Rd., Shanghai 200120, P. R. China

Dr. C. Hu

Department of Chemistry, State Key Laboratory of Molecular Engineering of Polymers, Shanghai Key Laboratory of Molecular Catalysis and Innovative Materials, Fudan University, 220 Handan Rd., Shanghai 200433, P. R. China.

Dr. Y. Lv

College of Chemical Engineering, Zhejiang University of Technology, Hangzhou 310014, P. R. China.

Table of Contents

Figure S14. SEM image of Ni-TABQ@*δ*-MnO_2 morphology evolution: (a) Pristine (b) After cycles.

Figure S15. Radar diagram of overall comparison of battery performance between *δ*-MnO_2, Ni-*δ*-MnO_2, and Ni-TABQ@*δ*-MnO_2.

Figure S16. The optical image of an LED toy powered by three Zn||Ni-TABQ@*δ*-MnO_2 cells integrated in series.

Figure S17. CV curves at different scan rates: (a) *δ*-MnO_2, (b) Ni-*δ*-MnO_2, (c) Ni-TABQ@*δ*-MnO_2 and (d) Ni-TABQ.

Figure S18. Charge transfer/storage kinetics of Ni-*δ*-MnO_2 cathode. (a) b values, (b) Capacitive contribution, (c) Ratios of Capacitive and diffusion-controlled contributions at various scan rates.

Figure S19. Charge transfer/storage kinetics of *δ*-MnO_2 cathode. (a) b values, (b) Capacitive contribution, (c) Ratios of Capacitive and diffusion-controlled contributions at various scan rates.

Figure S20. *Ex*-situ XRD patterns of hybrid superlattice Ni-TABQ@*δ*-MnO_2 cathode at specific discharge/charge states.

Figure S21. Schematic diagram of *in*-situ pH test device.

Figure S22. SEM images of Ni-TABQ@*δ*-MnO_2 cathode at different discharge/charge states.

Figure S23. GITT curves of *δ*-MnO_2-based cathodes during the discharge/charge process: (a) *δ*-MnO_2, (b) Ni-*δ*-MnO_2, (c) Ni-TABQ@*δ*-MnO_2.

Figure S24. Mn 2p XPS spectra of *δ*-MnO_2, Ni-*δ*-MnO_2, and Ni-TABQ@*δ*-MnO_2 cathodes at (a) fully discharged and (b) charged states. (c) GCD curves at 0.2 A g^{-1} of *δ*-MnO_2, Ni-*δ*-MnO_2 and Ni-TABQ@*δ*-MnO_2 in HOTF-H_2O electrolyte. (d) Operando FT-IR spectra of Ni-TABQ@*δ*-MnO_2 during the (dis)charge process.

Figure S25. SEM images of *δ*-MnO_2-based cathodes at full discharge states: (a) *δ*-MnO_2, (b) Ni-TABQ@*δ*-MnO_2. (c) The proportion of proton storage of Ni-TABQ@*δ*-MnO_2 cathode at different discharge current density.

Figure S26. The charge carries migration states of (a) Zn^{2+} and (b) H^+.

Table S1. Comparison of rate capacity (C_m), energy density (E), and cycling performance of recently reported Mn-based ZIBs in the literature.

Table S2. Zn/Mn ratio obtained for the fully charged of Ni-TABQ@δ-MnO2 cathode from Inductively Coupled Plasma Optical Emission Spectroscopy (ICP-OES) analysis.

Section S1. Experimental Procedures

1.1 Material Synthesis.

Synthesis of *δ*-MnO_2 and Ni-*δ*-MnO_2: *δ*-MnO_2 was synthesized using a simple hydrothermal method. In detail, 1.5 mmol of $KMnO_4$ and 1.5 mmol of $MnSO_4$ were dissolved in 60 mL of deionized water. The resulting solution was transferred to a 100 mL Teflon-lined stainless-steel autoclave and heated at 180 °C for 24 hours. Similarly, Ni-*δ*-MnO_2 was synthesized following the same procedure except by adding 0.3 mmol of $Ni(NO_3)_2 \cdot 6H_2O$ to the solution.

Synthesis of Ni-TABQ@*δ*-MnO_2 and Ni-TABQ: To prepare Ni-TABQ@*δ*-MnO_2, 291 mg of Ni-*δ*-MnO_2 was dispersed in the mixture of 30 mL of dimethyl sulfoxide (DMSO) and 3 mL of concentrated ammonia solution (~14 M) under vigorous stirring. Separately, 168 mg of 2,3,5,6-tetraamino-1,4-benzoquinone (TABQ, purchased from Adamas-Beta) was dissolved in 30 mL of DMSO and then added dropwise to the Ni-*δ*-MnO_2 dispersion solution while stirring continuously. The reaction mixture was allowed to proceed at room temperature for 8 hours under N_2 atmosphere. The resulting products was thoroughly washed several times with deionized water and acetone and subsequently dried in a vacuum oven at 80 °C for 12 hours (84.7% yield). Similarly, Ni-TABQ was synthesized following the same procedure except by replace Ni-*δ*-MnO_2 with 0.3 mmol of $Ni(NO_3)_2 \cdot 6H_2O$.

1.2 Characterizations.

The X-ray diffraction (XRD) patterns recorded on Rigaku Ultima IV with Cu radiation of 1.5418 Å were used to identify the crystal structure of the material. Field-emission scanning electron microscopy (SEM, Hitachi S-4800) and transmission electron microscopy (TEM, JEM-2100) equipped with an X-ray energy dispersive spectroscopy (EDS) instrument were used to investigate the morphologies and elemental maps. An X-ray photoelectron spectrometer (XPS, AXIS Ultra DLD) was employed to test surface element composition and state of products. Fourier-transformed infrared (FT-IR) spectrum was obtained by a Thermo Nicolet NEXUS spectrometer. Thermal stability was examined

in an air atmosphere using STA409 PC thermogravimetric (TG) analyzer at a heating rate of 10 °C min^{-1}.

For *ex-situ* characterizations including XRD, XPS, SEM, and TEM were utilized to study the phase transition and surface chemistry of the cathode. The cathodes were collected as follows: first, the batteries were disassembled at specific voltages during the (de-)charging process, then the electrodes were repeatedly washed with distilled water to ensure that glass fibers and residual electrolytes were removed from the surface. Finally, the electrodes were dried in a vacuum oven at 60 °C overnight to avoid oxidization of the samples.

1.3 Electrochemical Measurements.

The cathode was prepared through the mixture of Ni-TABQ@δ-MnO_2 active material (70 wt%), acetylene black (20 wt%), polytetrafluorethylene binder (10 wt%), and ground into a uniform slurry then coated on a titanium foil. The cathodes were dried at 110 °C for 12 h under a vacuum condition, and the mass loading of the electroactive material was approximately 2.5 mg cm^{-2}. 2 M $ZnSO_4$ + 0.2 M $MnSO_4$ electrolytes, Zn metal anode (> 99.99%), and glass fiber separator were coupled into a 2032 coin-type cell. The galvanostatic charge/discharge (GCD), rate performance, and cycle stability were performed on Neware battery test system (CT-4008Tn-5V10mA-164, Shenzhen, China). Cyclic voltammetry (CV) and electrochemical impedance spectroscopy (EIS) measurements with an amplitude of 0.005 V and a test frequency of 10^{-2}–10^{6} Hz were conducted on an electrochemical workstation (CHI660E). The specific capacity (C_m, mAh g^{-1}) can be evaluated from the GCD curves using the following form:

$$C_m = \frac{I \times \Delta t}{m} \qquad \text{(Eq. S1)}$$

Where I refer to the current density (A), Δt represents the discharging time (s), and m is the mass of the loading cathode (g).

The energy density (E, Wh kg^{-1}) and power density (P, W kg^{-1}) are calculated according to the following equations:

$$E = C_m \times \Delta V \qquad \text{(Eq. S2)}$$

$$P = \frac{E}{1000 \times \Delta t} \quad \text{(Eq. S3)}$$

Where ΔV is the voltage window (V), Δt represents the discharging time (h).

The in-situ pH battery system consists of a 1 × 1 cm^2 cathode with a mass loading of 2.5 mg cm^{-2}, alongside a rectangular zinc foil of equal area serving as the anode. This battery configuration is assembled within a 5 mL beaker equipped with magnetic stirring to ensure uniformity of the electrolyte during the reaction. The pH meter probe is inserted between the positive and negative electrodes to measure the pH of the electrolyte. The 3–3.5 mL of 2 M $ZnSO_4$ + 0.5 M $MnSO_4$ electrolyte were added to the beaker. Electrochemical testing was performed on a Neware battery test system at 0.5 A g^{-1} current density. The pH of the electrolyte was recorded using pH meter (INESA Scientific Instrumentco., Ltd, PHS-3E). The assembled in–situ pH battery system is illustrated in Figure S19.

Galvanostatic intermittent titration technique (GITT) measurements were used to calculate the diffusion coefficient of zinc ions ($D_{Zn^{2+}}$) in cathode based on the following equation:

$$D_{Zn^{2+}} = \frac{4}{\pi\tau}\left(\frac{mV}{MA}\right)^2\left(\frac{\Delta E_s}{\Delta E_t}\right)^2 \quad \text{(Eq. S4)}$$

where m (g) and M (g mol^{-1}) are assigned to the loading mass and molecular weight of active material; V (cm^3 mol^{-1}) represents the molar volume of materials deduced from crystallographic data; τ (s) is constant current pulse time; A (cm^2) is the surface area of electrode; ΔE_s (V) and ΔE_t (V) denote the change of steady-state voltage and the total change of the voltage during a constant pulse for a single-step GITT curve, respectively.

Electrochemical quartz crystal microbalance (EQCM) measurements were conducted by using a QCM 200 (Stanford Research Systems) and a BioLogic potentiostat. EQCM curves were recorded during the discharge process by CV scan at 1 mV s^{-1}. The mass change (Δm, g) of the electrode can be calculated by equation (5), where ρq and μq stands for the density (2.648 g cm^{-3}) and shear modulus (2.947 × 1011 g cm^{-1} s^{-2}) of quartz, respectively. f_0 (Hz) is the fundamental resonance frequency

of quartz. Δm (g) and Δf (Hz) are the mass change and frequency change, respectively. C_f (14.6 ng/Hz) is the sensitivity factor calculated by the relation based on frequency and mass change between the quartz crystal before and after coating. The molar weight of charge carrier (Mw) can be calculated according to equation (6), where F stands for the Faraday constant (96485 C mol^{-1}), n stands for the valence number of the ion, and ΔQ (C) stands for the charges passed through during the electrochemical process.

$$\Delta m = \frac{\sqrt{\rho_q \mu_q}}{2f_0} * \Delta f = -C_f * \Delta f \qquad \text{(Eq. S5)}$$

$$M_w = \frac{nf\Delta m}{\Delta Q} \qquad \text{(Eq. S6)}$$

Section S2. Calculation Methods

2.1 Density Functional Theory (DFT) Calculation.

All the DFT calculations of crystal structure are performed by the Vienna Ab initio Simulation Package (VASP)[S1] with the projector augmented wave (PAW) method.[S2] The exchange-functional is treated using the generalized gradient approximation (GGA) with Perdew-Burke-Emzerhof (PBE) functional.[S3] The energy cutoff for the plane wave basis expansion was set to be 400 eV. The Brillourin zone was sampled with Monkhorst mesh of 1×1×1 for the optimization for all the structures. All geometrical structures were fully optimized to its ground state. The convergence criteria for the total energy and the maximum force on each atom are less than 1×10^{-6} eV and 0.02 eV/Å, respectively. The charge density differences were simulated by VASPKIT code.[S4] The charge density differences between charge carriers and as-built crystal structure were simulated, of which the charge transfer level between both was calculated by a Bader charge analysis procedure. In addition, the climbing image nudged elastic band (CI-NEB) method[S5] was used to determine the minimum energy diffusion pathways of ions and the corresponding energy barriers. The uptake energy was calculated according to the following form:

$$\Delta E = E_{A/B} - E_B - E_A \qquad \text{(Eq. S7)}$$

The electron localization function (ELF) and independent gradient model (IGM) were calculated by using Multiwfn 3.8 programs.[S6] The simulations were conducted via the Multiwfn program to investigate the type of interaction force when the value of sign(λ2)ρ approaches zero and the VMD software was employed to plot the color-filled isosurface graphs IGM maps.[S7]

2.2 Activation Energy.

The activation energy (E_a, eV) of the charge transfer process was calculated from the Arrhenius equation:

$$1/R_{ct} = A\exp(-E_a/RT) \qquad \text{(Eq. S8)}$$

Where R_{ct} is the charge transfer resistance (Ω), A is a constant in a stable experimental condition, R is the gas constant (8.314 J mol^{-1} K^{-1}). Plot $\ln(R_{ct}^{-1})$ *vs.* $1000/T$ and fit it linearly to obtain E_a:

$$\ln(R_{ct}^{-1}) = -E_a/RT + k \quad \text{(Eq. S9)}$$

Where k is a constant.

2.3 Charge Storage Kinetics.

The sweep rate (v) and peak current (i) of ZHCs batteries were investigated based on the form:

$$i = av^b \quad \text{(Eq. S10)}$$

they can be established by calculating the equation that follows between i and V:

$$i = k_1v + k_2v^{1/2} \quad \text{(Eq. S11)}$$

Where k_1 and k_2 are constants, k_1v represents the fast-capacitive process, and $k_2v^{1/2}$ accounts for the diffusion-controlled process.

The combined series resistances (R_s) can be extracted from the intersection of the curve and horizontal axis, comprising the electrolyte ionic resistance, electrode/electrolyte interface resistance, and active material electronic resistance. The charge-transfer resistance (R_{ct}) refers to the radius of semicircles in the curves of Nyquist plots. The capacitance C (ω) changes along with the frequency which is defined as follows:

$$C(\omega) = C'(\omega) - jC''(\omega) \quad \text{(Eq. S12)}$$

$$C'(\omega) = -Z''(\omega) / (\omega \left| Z(\omega) \right|^2) \quad \text{(Eq. S13)}$$

$$C''(\omega) = Z'(\omega) / (\omega \left| Z(\omega) \right|^2) \quad \text{(Eq. S14)}$$

Where C′ (ω) is the real part of C (ω), the low frequency value of C' (ω) refers to the capacitance of the device tested in constant-current discharge process; C'' (ω) is the imaginary part associated with the energy dissipation by an irreversible process leading to a hysteresis, $Z'(\omega)$ and $Z''(\omega)$ are the real and imaginary parts of the complex impedance Z (ω), respectively. ω is the angular frequency given by $\omega = 2\pi f$. The relaxation time constant (τ_0) is calculated by equation:

$$\tau_0 = 1/f_0 \quad \text{(Eq. S15)}$$

τ_0 is marked at the position where the imaginary part of the capacitance (C'') reaches its maximum at frequency f_0.

Section S3. Supplementary Characterizations

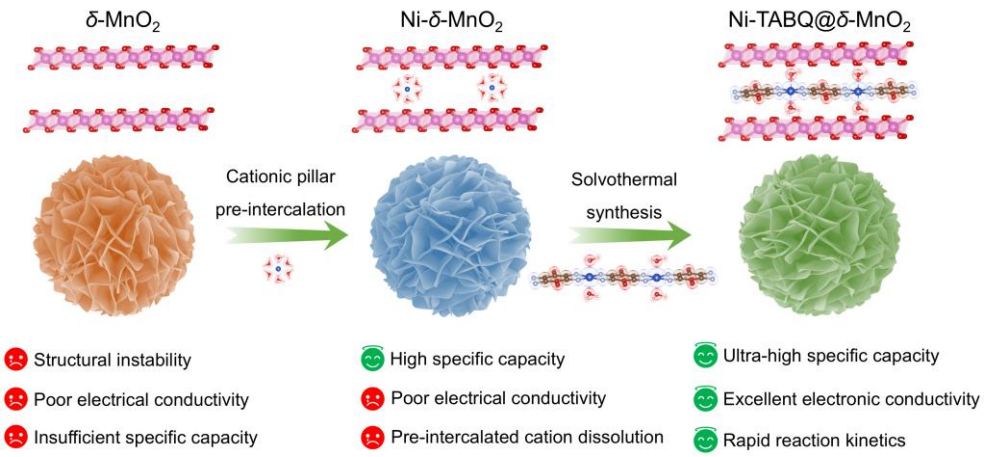

Figure S1. Synthesis diagram of hybrid superlattice Ni-TABQ@δ-MnO_2.

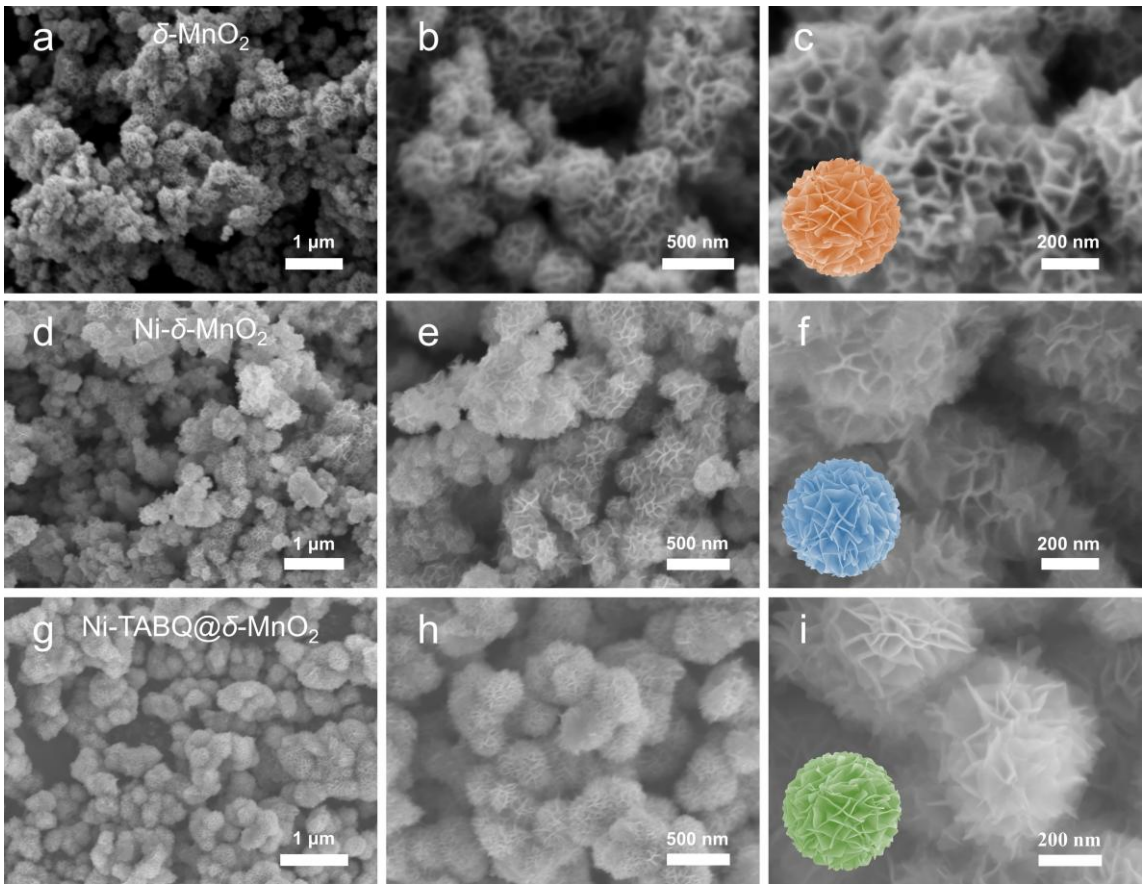

Figure S2. SEM images of (a-c) δ-MnO_2, (d-e) Ni-δ-MnO_2, (g-i) Ni-TABQ@δ-MnO_2.

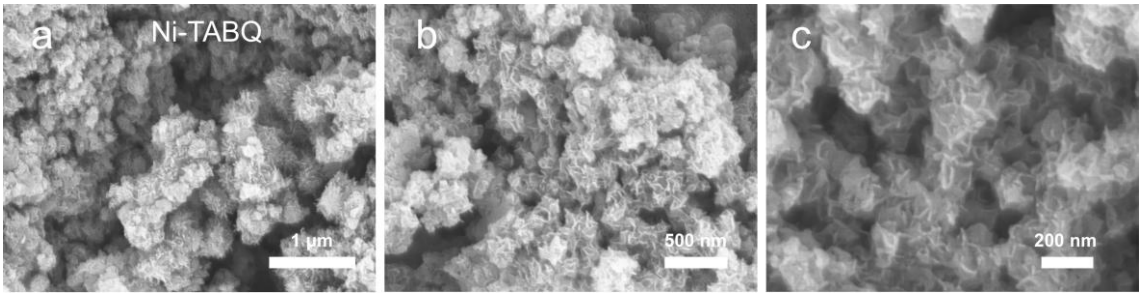

Figure S3. SEM images of (a-c) Ni-TABQ.

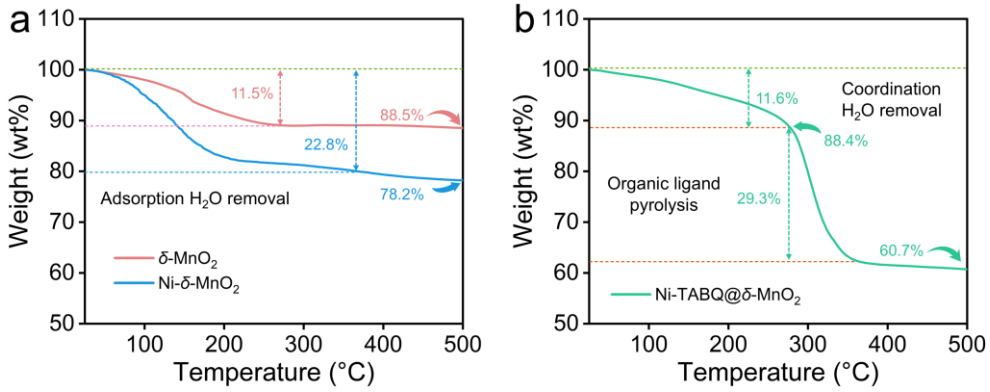

Figure S4. TG curves of (a) *δ*-MnO_2, Ni-*δ*-MnO_2 and (b) Ni-TABQ@*δ*-MnO_2 cathodes.

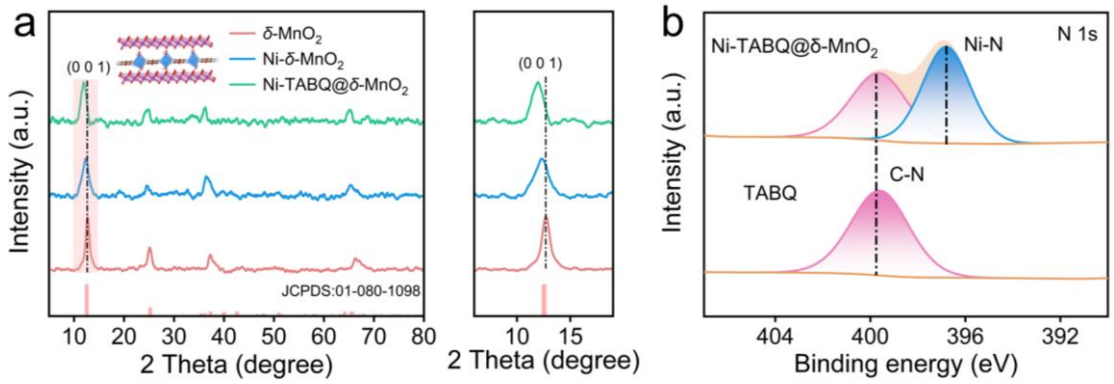

Figure S5. (a) XRD patterns of *δ*-MnO_2, Ni-*δ*-MnO_2, and hybrid superlattice Ni-TABQ@*δ*-MnO_2 cathodes. (b) XPS spectra of N 1s for TABQ and Ni-TABQ@*δ*-MnO_2.

<u>Notes to Figure S5:</u> XPS spectra indicate the absence of Ni-N bonds, which directly confirm the bonding of Ni^{2+} cations with TABQ in Ni-TABQ@*δ*-MnO_2 host (Figure S5b).

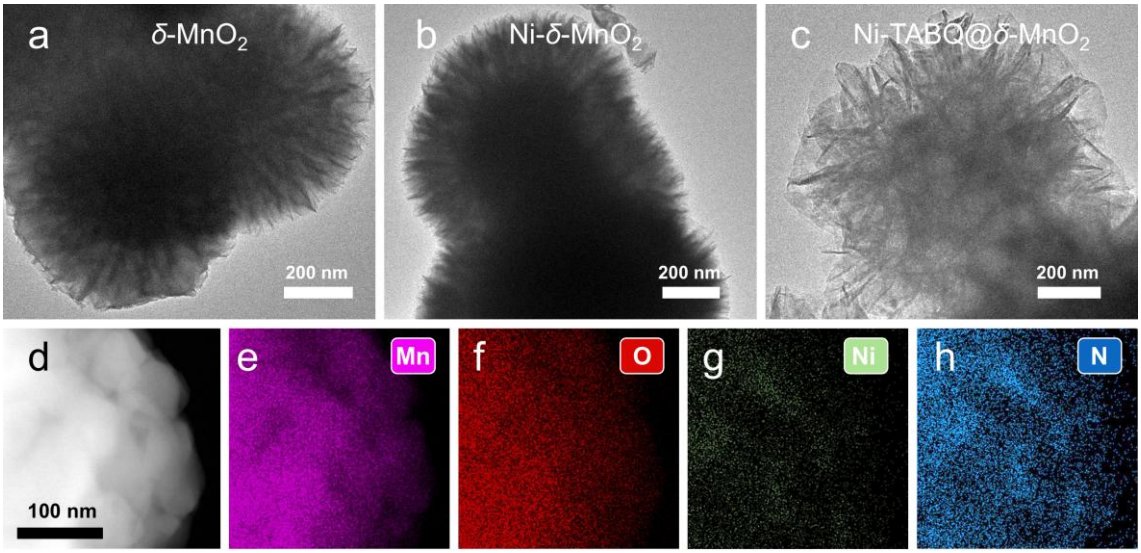

Figure S6. TEM images of (a) *δ*-MnO_2, (b) Ni-*δ*-MnO_2, (c) Ni-TABQ@*δ*-MnO_2. TEM-mapping images of Ni-TABQ@*δ*-MnO_2.

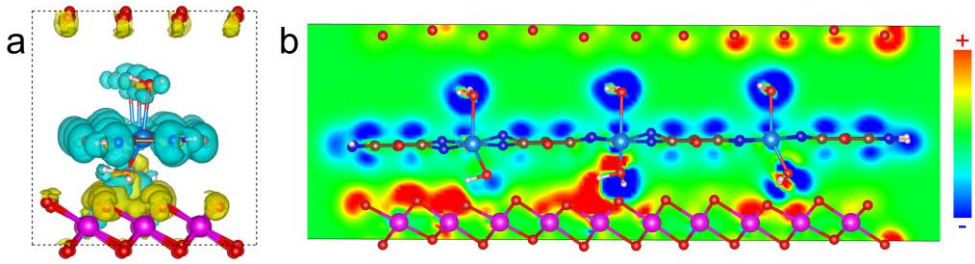

Figure S7. (a) side view of the differential electron density isosurfaces and (b) 2D contour maps of differential charges of Ni-TABQ@*δ*-MnO_2.

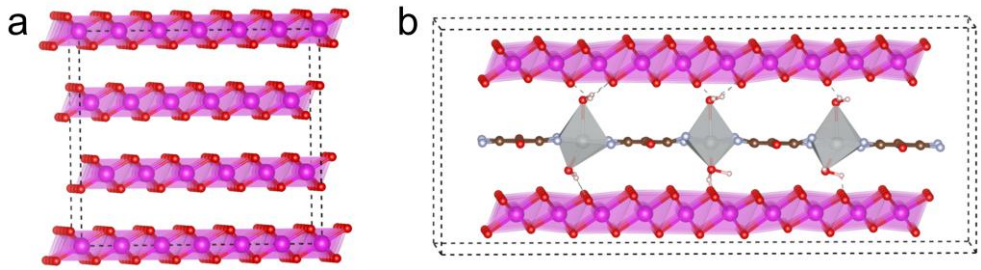

Figure S8. Crystal structure model of (a) *δ*-MnO_2 and (b) Ni-TABQ@*δ*-MnO_2.

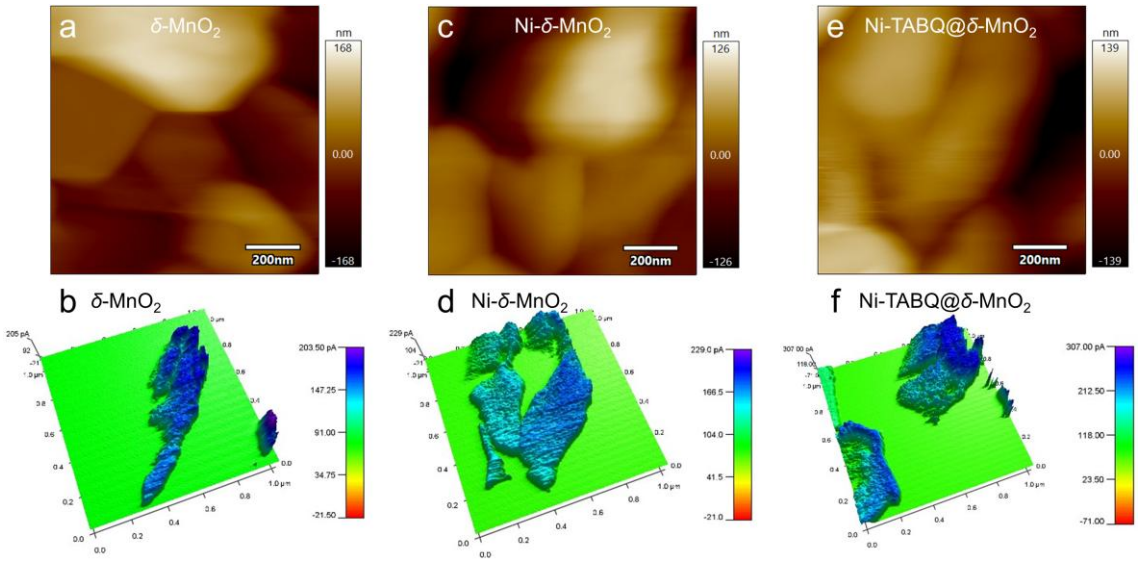

Figure S9. The morphology and surface current distribution of CAFM. (a, b) *δ*-MnO_2, (c, d) Ni-*δ*-MnO_2, (e, f) Ni-TABQ@*δ*-MnO_2.

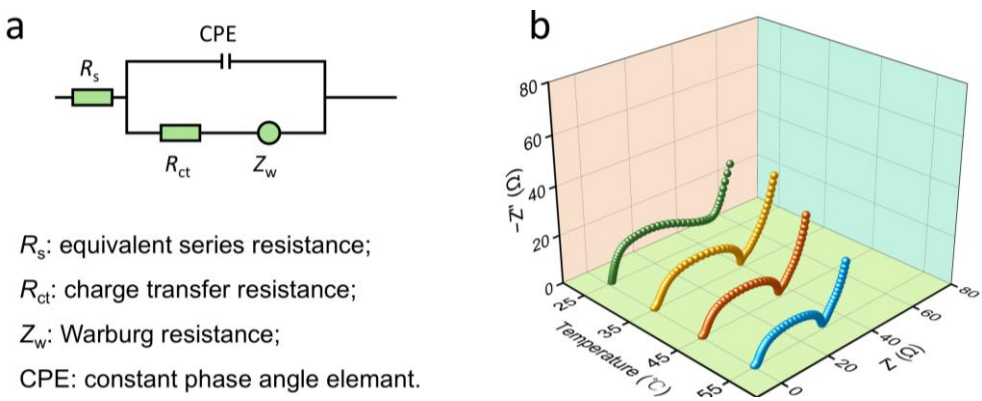

Figure S10. (a) Equivalent circuit of Nyquist plots. (b) Electrochemical impedance spectroscopies (EIS) of Ni-TABQ@*δ*-MnO_2 at different operation temperatures for calculating the activation energy.

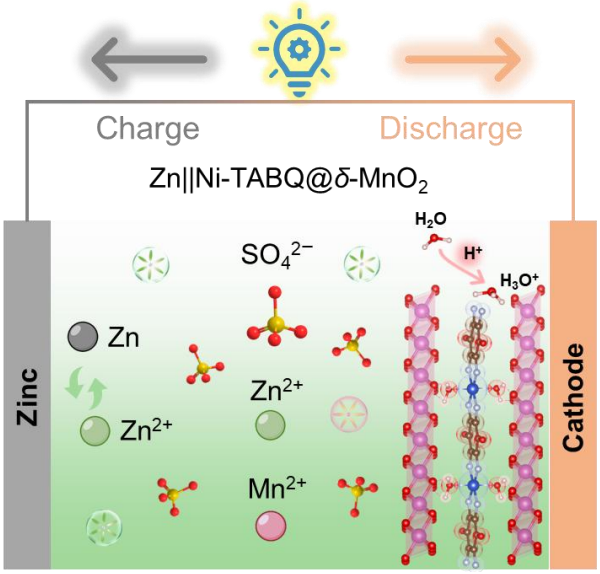

Figure S11. Operation mechanism diagram of Zn||Ni-TABQ@δ-MnO_2 battery.

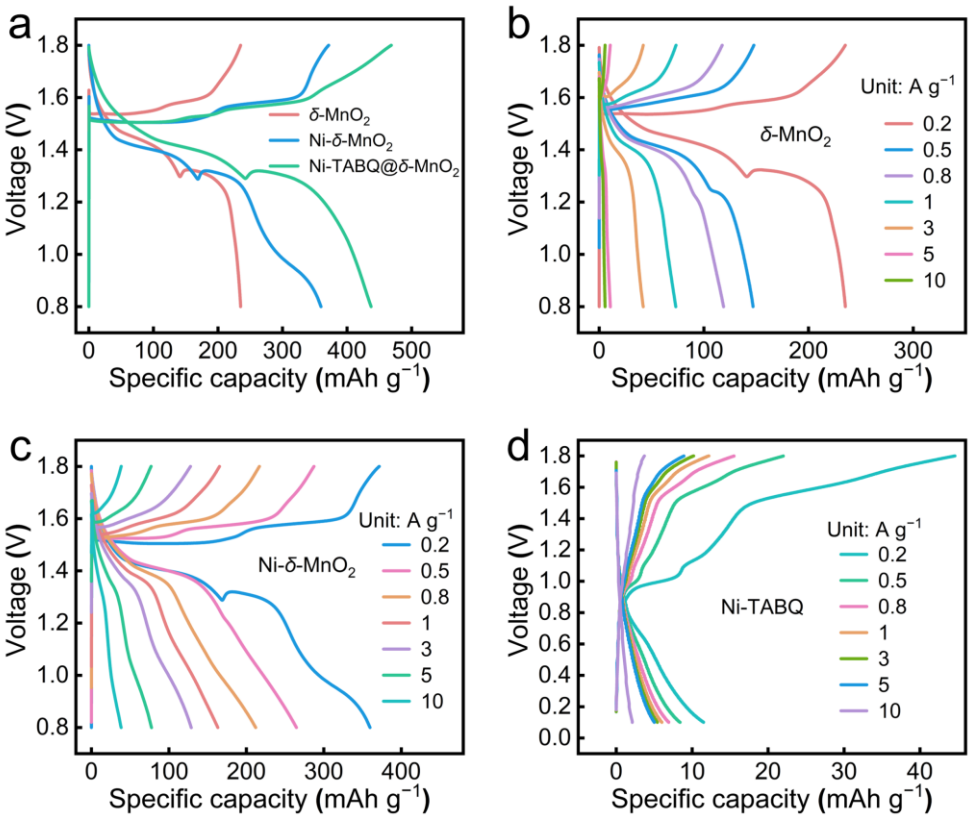

Figure S12. GCD curves. (a) Comparison of different cathodes at 0.2 A g^{-1}. (b) δ-MnO_2, (c) Ni-δ-MnO_2 and (d) Ni-TABQ.

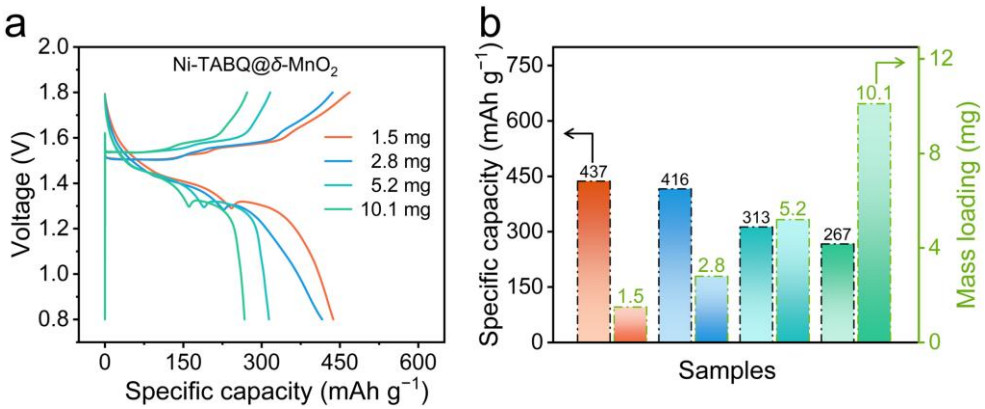

Figure S13. (a) GCD profiles of Ni-TABQ@*δ*-MnO_2 cathode at different mass loading. (b) Comparison of specific capacity at different mass loading.

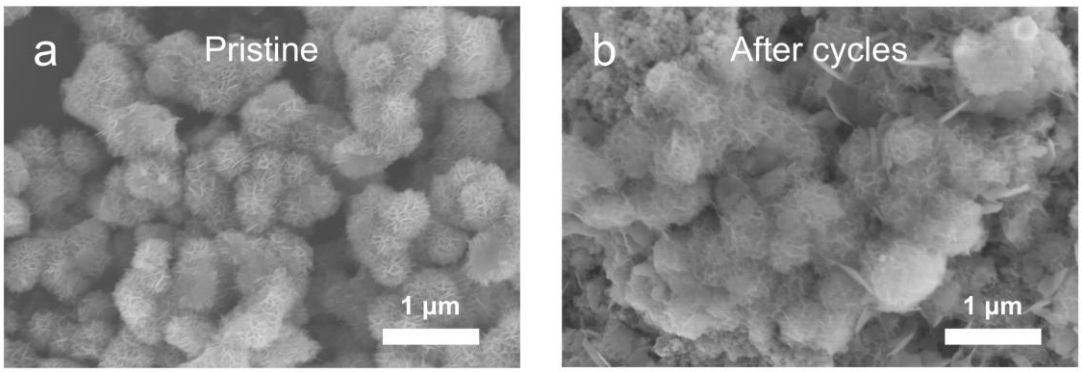

Figure S14. SEM image of Ni-TABQ@*δ*-MnO_2 morphology evolution. (a) Pristine (b) After cycles.

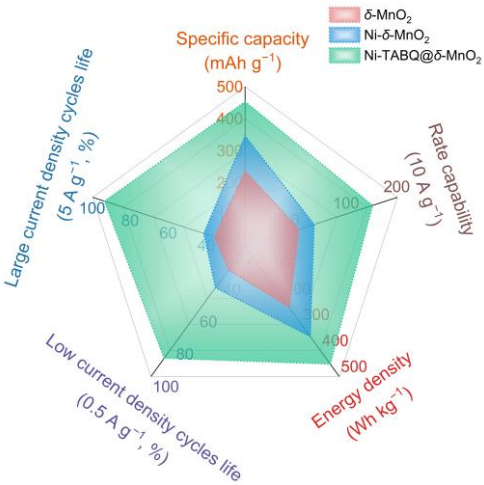

Figure S15. Radar diagram of overall comparison of battery performance between *δ*-MnO_2, Ni-*δ*-MnO_2, and Ni-TABQ@*δ*-MnO_2.

Figure S16. The optical image of an LED toy powered by three Zn||Ni-TABQ@*δ*-MnO_2 cells integrated in series.

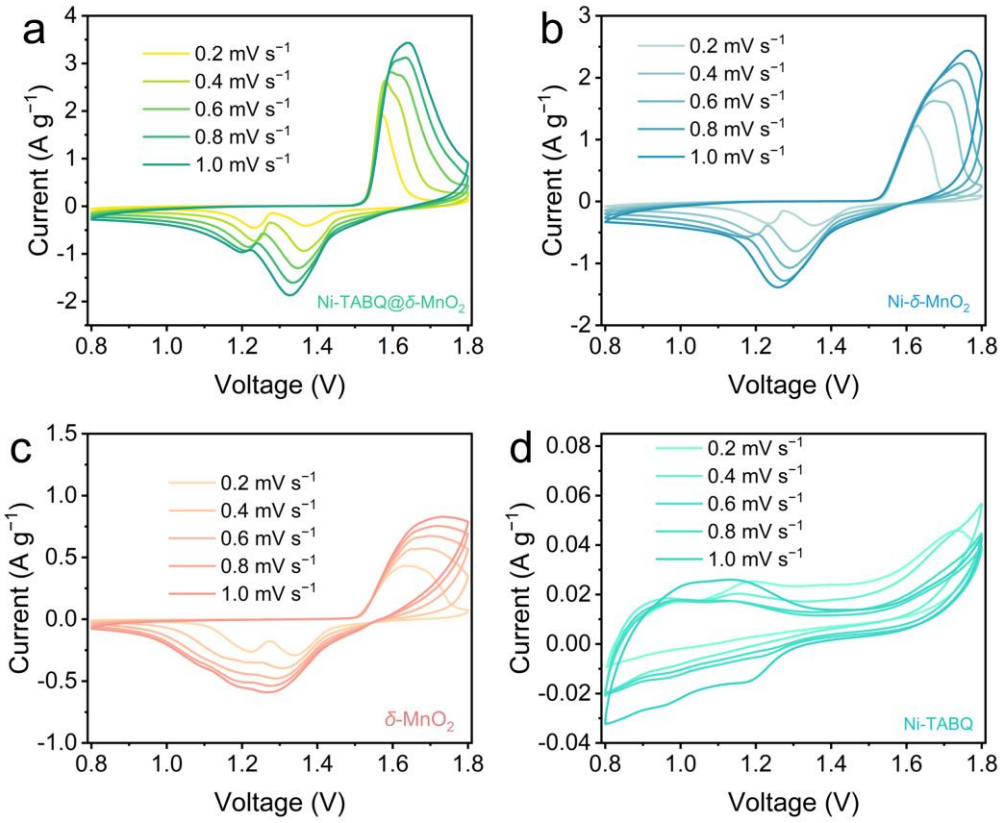

Figure S17. CV curves at different scan rates: (a) *δ*-MnO_2, (b) Ni-*δ*-MnO_2, (c) Ni-TABQ@*δ*-MnO_2 and (d) Ni-TABQ.

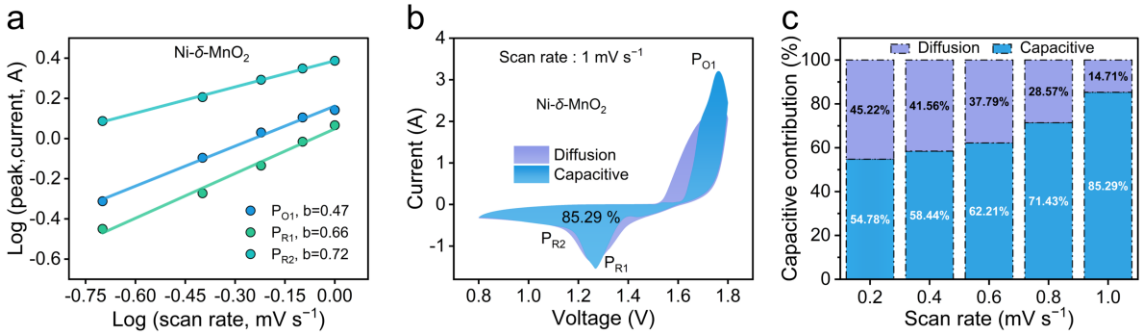

Figure S18. Charge transfer/storage kinetics of Ni-*δ*-MnO_2 cathode. (a) b values, (b) Capacitive contribution, (c) Ratios of capacitive and diffusion-controlled contributions at various scan rates.

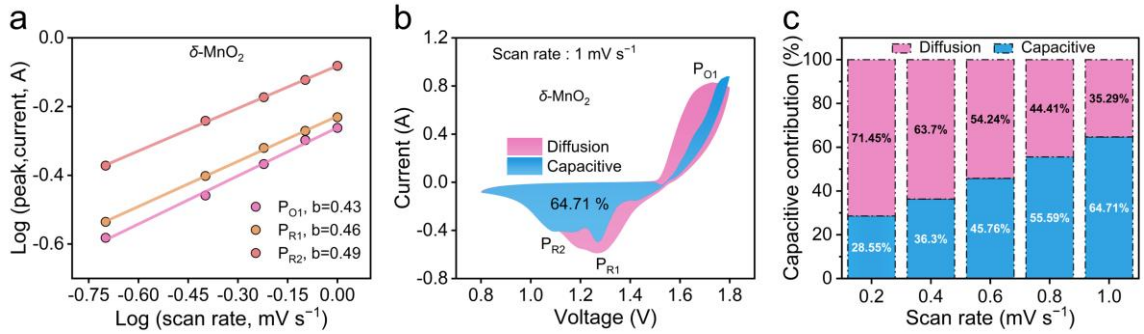

Figure S19. Charge transfer/storage kinetics of *δ*-MnO_2 cathode. (a) b values, (b) Capacitive contribution, (c) Ratios of capacitive and diffusion-controlled contributions at various scan rates.

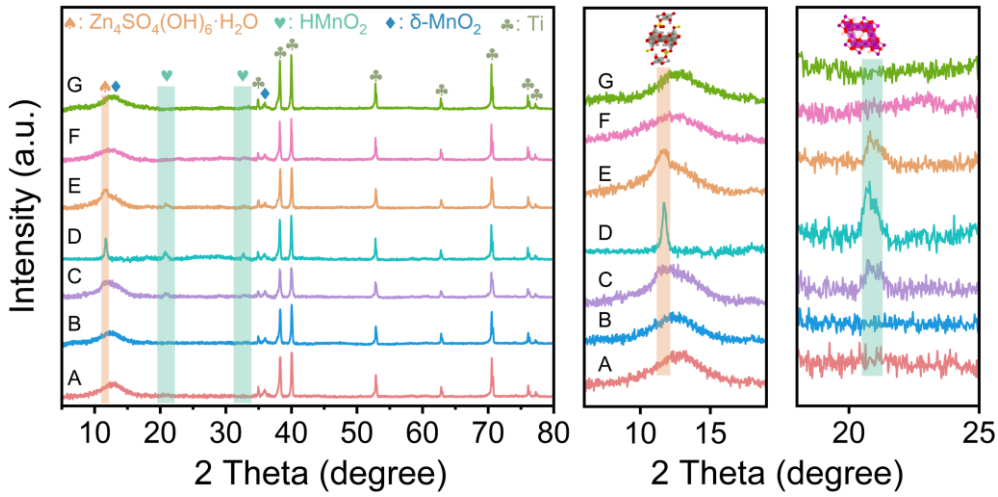

Figure S20. *Ex*-situ XRD patterns of hybrid superlattice Ni-TABQ@*δ*-MnO_2 cathode at specific discharge/charge states.

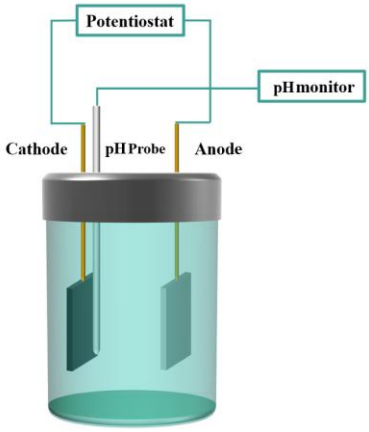

Figure S21. Schematic diagram of *in*-situ pH test device.

Notes to Figure S21: In the *in*-situ pH test device, a two-electrode Zn||Ni-TABQ@*δ*-MnO_2 cells was constructed with 2 M $ZnSO_4$ and 0.2 M $MnSO_4$ aqueous electrolyte and *in*-situ pH monitoring was conducted to evaluate the variation in pH of the Ni-TABQ@*δ*-MnO_2 cathode surface at various (dis)charged states. To track the most accurate pH response, the pH meter's glass electrode is attached to the cathode's surface.

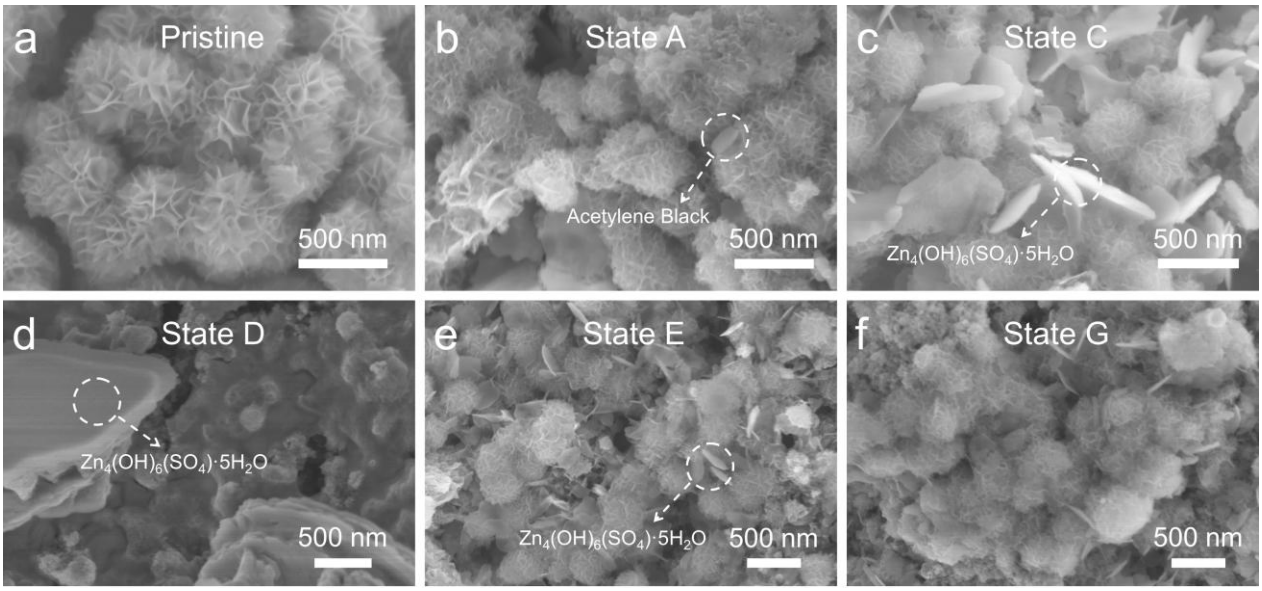

Figure S22. SEM images of Ni-TABQ@*δ*-MnO_2 cathode at different discharge/charge states.

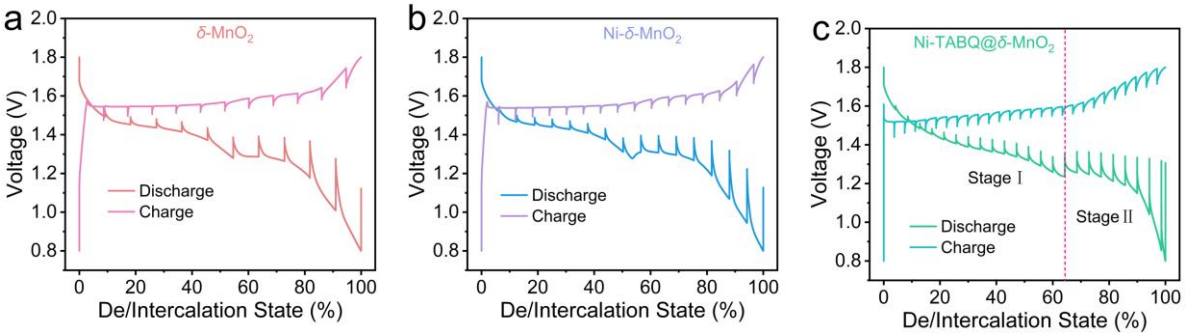

Figure S23. GITT curves of δ-MnO_2-based cathodes during the discharge/charge process: (a) δ-MnO_2, (b) Ni-δ-MnO_2, (c) Ni-TABQ@δ-MnO_2.

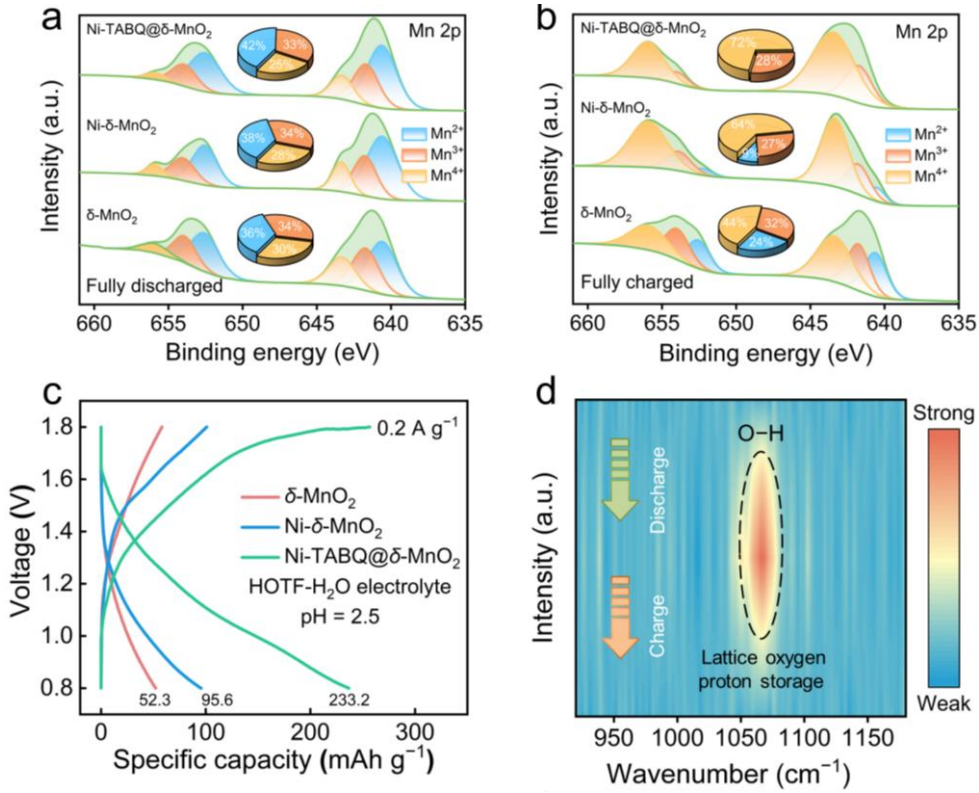

Figure S24. Mn 2p XPS spectra of δ-MnO_2, Ni-δ-MnO_2, and Ni-TABQ@δ-MnO_2 cathodes at (a) fully discharged and (b) charged states. (c) GCD curves at 0.2 A g^{-1} of δ-MnO_2, Ni-δ-MnO_2 and Ni-TABQ@δ-MnO_2 in HOTF-H_2O electrolyte. (d) Operando FT-IR spectra of Ni-TABQ@δ-MnO_2 during the (dis)charge process.

<u>Notes to Figure S24:</u> Operando FT-IR spectra show the generation/disappearance of O−H signals, which derive from reaction between the lattice oxygen of Ni-TABQ@δ-MnO_2 and protons (Figure S24d). Such a result confirms proton participation through distinct shifts in O−H stretching bands during the (dis)charge process.

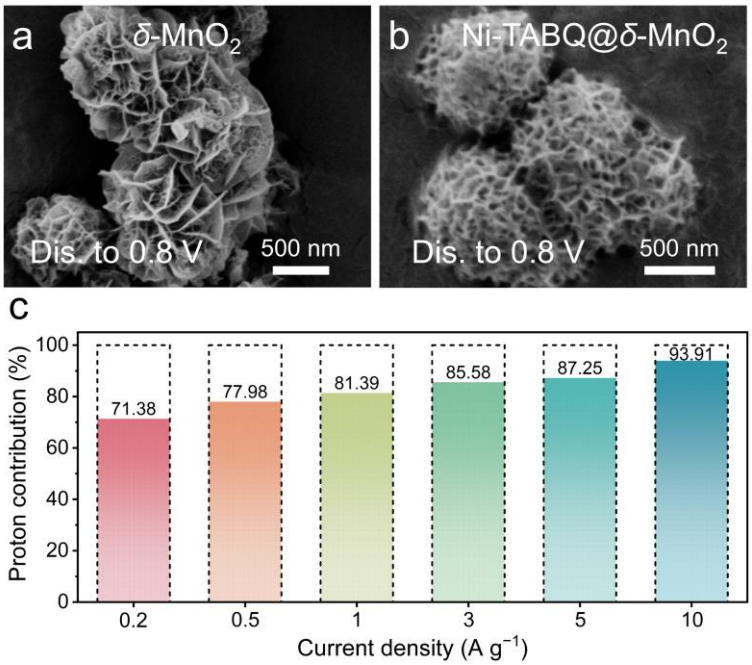

Figure S25. SEM images of *δ*-MnO_2-based cathodes at full discharge states. (a) *δ*-MnO_2, (b) Ni-TABQ@*δ*-MnO_2. (c) The proportion of proton storage of Ni-TABQ@*δ*-MnO_2 cathode at different discharge current density.

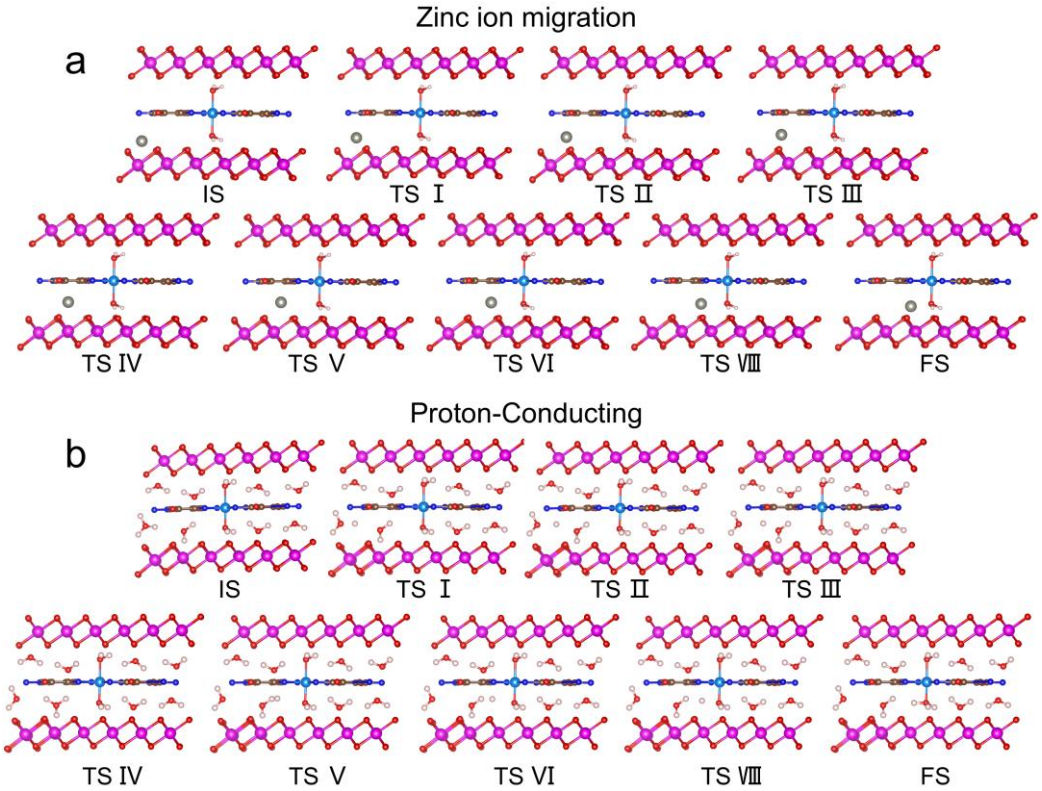

Figure S26. The charge carries migration states of (a) Zn^{2+} and (b) H^{+}.

Table S1 Comparison of rate capacity (C_m), energy density (E), and cycling performance of recently reported Mn-based ZIBs in the literature.

Cathode	Electrolyte	C_m (mAh g^{-1})	E (Wh kg^{-1})	Lifespan	Refs.
Ni-TABQ@δ-MnO_2	2M $ZnSO_4$ + 0.2M $MnSO_4$	453@0.2 A g^{-1} 152@10 A g^{-1}	586	93.82%, 8,000 cycles (3 A g^{-1})	This work
Mn_2O_3	3M $ZnSO_4$ + 0.2M $MnSO_4$	228@0.1 A g^{-1} 88@5 A g^{-1}	311	82%, 2000 cycles (2 A g^{-1})	[S8]
Ni-Mn_2O_3	2M $ZnSO_4$	252@0.1 A g^{-1} 132@1 A g^{-1}	328	85.6%, 2500 cycles (1 A g^{-1})	[S9]
α-MnO_2	2M $ZnSO_4$ + 0.1M $MnSO_4$	285@1/3 C 113@10 C	170	92%, 5000 cycles (5 C)	[S10]
δ-MnO_2	2M $ZnSO_4$ + 0.1M $MnSO_4$	288.8@0.1 A g^{-1} 85.7@1 A g^{-1}	389	91.9%, 1500 cycles (1 A g^{-1})	[S11]
MnO_2@CFP	2M $ZnSO_4$ + 0.1M $MnSO_4$	290@1/3 C 174@6.5 C	288	~100%, 10000 cycles (6.5 C)	[S12]
Bi-MnO_2	2M $ZnSO_4$ + 0.2M $MnSO_4$	363@0.1 A g^{-1} 103@3 A g^{-1}	486	93%, 10000 cycles (1 A g^{-1})	[S13]
S-MnO_2	2M $ZnSO_4$ + 0.1M $MnSO_4$	324@0.1 A g^{-1} 205@2 A g^{-1}	412	73%, 1000 cycles (3 A g^{-1})	[S14]
$ZnMn_2O_4$	2M $ZnSO_4$ + 0.1M $MnSO_4$	318.4@0.1 A g^{-1} 157.7@1 A g^{-1}	408	86.4%, 1500 cycles (1 A g^{-1})	[S15]
$Mg_{0.9}Mn_3O_7 \cdot 2.7H_2O$	3M $ZnSO_4$ + 0.1M $MnSO_4$	312@0.2 A g^{-1} 132@5 A g^{-1}	418	92%, 5000 cycles (5 A g^{-1})	[S16]

Mn_2O_3-$ZnMn_2O_4$	2M $Zn(CF_3SO_3)_2$ + 0.1M $MnSO_4$	247.4@0.1 A g^{-1} 120.2@5 A g^{-1}	305	93.3%, 2000 cycles (3 A g^{-1})	[S17]
CaMnO-140	10M LiTFSI + 1M $Zn(CF3SO3)_2$	485.4@0.1 A g^{-1} 154.5@10 A g^{-1}	592	90.6%, 5000 cycles (5 A g^{-1})	[S18]
Ru-MnO_2	2M $ZnSO_4$ + 0.1M $MnSO_4$	314.4@0.2 A g^{-1} 101.7@5 A g^{-1}	384	82.8%, 2000 cycles (1 A g^{-1})	[S19]

Table S2 Zn/Mn ratio obtained for the fully discharged Ni-TABQ@*δ*-MnO_2 cathode from inductively coupled plasma optical emission spectroscopy (ICP-OES) analysis.

Sample Ni-TABQ@*δ*-MnO_2	Zn (mmol L^{-1}) × 10^{-2}	Mn (mmol L^{-1}) × 10^{-2}	Zn/Mn Ratio	Proton Contribution
Fully charge	1.31	13.51	9.7%	N/A
Fully discharge (0.2 A g^{-1})	6.21	16.22	38.32%	71.38%
Fully discharge (0.5 A g^{-1})	4.89	15.44	31.72%	77.98%
Fully discharge (1 A g^{-1})	3.45	12.21	28.31%	81.39%
Fully discharge (3 A g^{-1})	4.47	18.57	24.12%	85.58%
Fully discharge (5 A g^{-1})	4.51	20.12	22.45%	87.25%
Fully discharge (10 A g^{-1})	2.59	16.54	15.77%	93.91%

Notes to Table S2: The ICP-OES analysis at fully charge and fully discharge states was selected to calculate the contribution from H^+ and Zn^{2+} of the Ni-TABQ@*δ*-MnO_2 cathode at different current density.

References

[S1] G. Kresse, J. Furthmüller, *Comput. Mater. Sci.* **1996**, *6*, 15.

[S2] P. E. Blöchl, *Phys. Rev. B* **1994**, *50*, 17953.

[S3] J. P. Perdew, J. A. Chevary, S. H. Vosko, K. A. Jackson, M. R. Pederson, D. J. Singh, C. Fiolhais, *Phys.*

Rev. B **1992**, *46*, 6671.

[S4] V. Wang, N. Xu, J.-C. Liu, G. Tang, W.-T. Geng, *Comput. Phys. Commun.* **2021**, *267*, 108033.

[S5] V. Ásgeirsson, B. O. Birgisson, R. Bjornsson, U. Becker, F. Neese, C. Riplinger, H. Jónsson, *J. Chem. Theory Comput.* **2021**, *17*, 4929.

[S6] T. Lu, F. Chen, *J. Comput. Chem.* **2012**, *33*, 580.

[S7] W. Humphrey, A. Dalke, K. Schulten, *J. Mol. Graph.* **1996**, *14*, 33.

[S8] Y. Ma, Y. Ma, T. Diemant, K. Cao, X. Liu, U. Kaiser, R. J. Behm, A. Varzi, S. Passerini, *Adv. Energy Mater.* **2021**, *11*, 2100962.

[S9] D. Zhang, J. Cao, X. Zhang, N. Insin, S. Wang, J. Han, Y. Zhao, J. Qin, Y. Huang, *Adv. Funct. Mater.* **2021**, *31* 2009412.

[S10] H. Pan, Y. Shao, P. Yan, Y. Cheng, K. S. Han, Z. Nie, C. Wang, J. Yang, X. Li, P. Bhattacharya, K. T. Mueller, J. Liu, *Nat. Energy* **2016**, *1*, 16039.

[S11] W. Lv, J. Meng, Y. Li, W. Yang, Y. Tian, X. Lyu, C. Duan, X. Ma, Y. Wu, *Nano Energy* **2022**, *98*, 107274.

[S12] W. Sun, F. Wang, S. Hou, C. Yang, X. Fan, Z. Ma, T. Gao, F. Han, R. Hu, M. Zhu, C. Wang, *J. Am. Chem. Soc.* **2017**, *139*, 9775.

[S13] Y. Ma, M. Xu, R. Liu, H. Xiao, Y. Liu, X. Wang, Y. Huang, G. Yuan, *Energy Storage Mater.* **2022**, *48*, 212.

[S14] Y. Zhao, P. Zhang, J. Liang, X. Xia, L. Ren, L. Song, W. Liu, X. Sun, *Energy Storage Mater.* **2022**, *47*, 424.

[S15] S. Deng, Z. Tie, F. Yue, H. Cao, M. Yao, Z. Niu, *Angew. Chem. Int. Ed.* **2022**, *61*, e202115877.

[S16] J. Li, N. Luo, L. Kang, F. Zhao, Y. Jiao, T. J. Macdonald, M. Wang, I. P. Parkin, P. R. Shearing, D. J. L. Brett, G. Chai, G. He, *Adv. Energy Mater.* **2022**, *12*, 2201840.

[S17] Y. Zeng, Y. Wang, Q. Jin, Z. Pei, D. Luan, X. Zhang, X. W. D. Lou, *Angew. Chem. Int. Ed.* **2021**, *60*, 25793.

[S18] T. Wang, J. Jin, X. Zhao, X. Qu, L. Jiao, Y. Liu, *Angew. Chem. Int. Ed.* **2024**, *63*, e202412057.

[S19] S. Wang, S. Yao, F. Zhang, K. Ji, Y. Ji, J. Li, W. Fu, Y. Liu, J. Yang, R. Liu, J. Xie, Z. Yang, Y.-M. Yan, *Angew. Chem. Int. Ed.* **2025**, *64*, e202415997.